Delft University of Technology

3-Axis Angular Strain Estimation With Hall Effect Sensors for Proprioception of Soft Robotic Manipulators

Adamu, Yusuf Abdullahi; Feliu-Talegon, Daniel; Mathew, Anup Teejo; Renda, Federico

Citation (APA)
Adamu, Y. A., Feliu-Talegon, D., Mathew, A. T., & Renda, F. (2025). 3-Axis Angular Strain Estimation With Hall Effect Sensors for Proprioception of Soft Robotic Manipulators. *IEEE Robotics and Automation Letters*, *10*(9), 8666-8673. https://doi.org/10.1109/LRA.2025.3588782

Important note
To cite this publication, please use the final published version (if applicable).
Please check the document version above.

3-Axis Angular Strain Estimation With Hall Effect Sensors for Proprioception of Soft Robotic Manipulators

Yusuf Abdullahi Adamu ⓘ, Daniel Feliu-Talegon ⓘ, *Member, IEEE*, Anup Teejo Mathew ⓘ, *Member, IEEE*, and Federico Renda ⓘ, *Member, IEEE*

Abstract—**Slender soft robots offer significant advantages for real-life applications, particularly in areas that require delicate and adaptable interaction with complex environments. However, their effectiveness and safety can be greatly limited in the absence of sensing capabilities. Hall effect sensors, known for their excellent sensitivity and compact design, offer an innovative solution for equipping soft manipulators with perceptive abilities. In this letter, we propose an optimized sensor-magnet arrangement that can estimate all 3 angular strains of a slender rod, including torsion and bending along orthogonal axes, using a single sensor-magnet pair. With optimized design and experimental data, we trained a neural network to accurately predict angular strains from the measured magnetic fields. Using the predicted strains at different points along the body, we reconstruct the 3D shape of the sensorized manipulator using a Piece-wise Constant Angular Strain (PCAS) model. Two manipulator designs were considered in this work: single-segment and three-segment. Experimental results indicate tip position errors of less than 2% of the total manipulator length for the single-segment soft robot and less than 5% for the three-segment soft robot. The inherent simplicity of our design enables easy scaling and replication while ensuring reliable strain measurements critical for accurate robot shape reconstruction.**

Index Terms—**Soft robots, Hall effect sensors, strain sensing, shape reconstruction, neural networks.**

I. INTRODUCTION

SOFT robots, inspired by flexible biological organisms, offer advantages such as flexibility, safety, and versatility, enabling them to perform tasks in applications like minimally invasive surgery, rescue operations, and underwater manipulation—areas often challenging for rigid robots.

Conventional sensing approaches are often unsuitable for soft robots due to their infinite degrees of freedom. Recent research focuses on embedded sensing over external methods like cameras, enabling real-time shape sensing with minimal impact on flexibility and improved performance [1], [2], [3].

Latest developments in sensing technologies have focused on achieving proprioception in soft robots by estimating curvature and strain. Various sensing techniques have been utilized, including resistive flex sensors [4], [5], IMU-based sensors [6], capacitive strain sensors [7], [8], fiber Bragg gratings (FBGs) [9], and conductive liquid metals [10]. Sensor selection depends on the application and conditions. Though resistive bend sensors and IMU-based sensors are low-cost and easy to fabricate, they are prone to drift over time and with temperature changes [11]. Capacitive sensors are hard to integrate and limited in range, while FBGs require complex hardware despite their high accuracy. Liquid metal-based sensors, typically using eutectic Gallium-Indium (eGaIn) [12], offer flexibility but are difficult to fabricate and reproduce. Many of these techniques rely on distributed sensing, which increases system complexity and computational load.

Other important shape-sensing methods for soft manipulators have been presented in [13], where changes in actuator length are used to estimate manipulator shape, while [14] incorporates actuator length and force to estimate the shape's pose and velocity. Notably, [13] demonstrated the ability to estimate torsional deformation. While effective, these approaches often require multiple tendons or strings and rely on optimization procedures to determine tendon routing and the number of tendons to reconstruct the shape. This increases mechanical complexity and reduces scalability.

Magnetic-based sensors, such as Hall effect and magnetoresistive devices, offer a compact, sensitive, and low-stiffness solution for shape sensing in soft robots, providing fast response and overcoming limitations of other sensing methods [15]. Motivated by these insights, we propose a method that embeds the sensor system directly within the soft material, offering a compact and robust solution that supports localized sensing and enables improved shape reconstruction accuracy without adding complexity to the actuation design.

A. Related Work

Early Hall effect-based sensing in soft manipulators focused on planar curvature estimation, using integrated magnets and Hall sensors on flexible circuit boards, achieving minimal estimation error for one-axis planar bending tasks [16]. Enhanced methods for detecting planar bending using magnetic sensors were proposed for continuum robotic manipulators in [17] and [18]. In these studies, quadratic and higher-order Bezier curves were employed to relate the movements of magnets to the positions of the sensors. However, these methods are limited by simplified proprioception models that only capture planar bending and do not account for torsional strain. These limitations reduce pose estimation accuracy and introduce added bulk and complexity due to reliance on external electromagnetic excitation. In [11], a probabilistic particle filter combined with magnetic simulation was employed to predict the planar bending of a cylindrical soft robot, with parameters including the bending angle and direction. Another approach that uses a linear magnetic encoder to estimate the curvature and tip position of a continuum manipulator was introduced in [19], but it also lacks the capability to measure out-of-plane deformations such as torsion. Recent studies have focused on the three-dimensional shape reconstruction of continuum robots. In [15], an elongation mode was added to the 2-axis planar bending of a soft manipulator. The method used in the study combines training a neural network architecture capable of learning the robot's 3D shape from magnetic field data with an optimization strategy for the configuration variables. This sensor-magnet arrangement marked the first departure from the conventional co-axial pair placements.

We identified the following research gaps from the previous sensing and shape reconstruction methods based on Hall-effect sensors:

- *Design Limitations:* Bulky or complex designs limit scalability and are often restricted to sensing planar bending. Multiple sensors or external excitation can cause crosstalk in complex deformations, reducing resolution and distorting signals.
- *Simplified Shape Reconstruction Models:* Models such as Bezier curve interpolation and Piecewise Constant Curvature (PCC) rely on the assumption of zero torsion, which restricts the accuracy of determining the true pose of the manipulator's tip.
- *Demonstration of Complex Deformations:* Previous studies are limited to simple bending with narrow deformation ranges, lacking demonstrations of local strain measurement or complex deformations.

B. Contributions

Many slender continuum robots undergo deformations primarily in 3 modes: torsion and bending in two orthogonal directions [20], [21], [22]. The configuration of these kinds of soft manipulators is more accurately represented when torsional deformation is incorporated into the shape reconstruction model [23], [24]. Our approach for sensorizing these soft manipulators using the Hall effect sensors contributes to the state-of-the-art in the following ways.
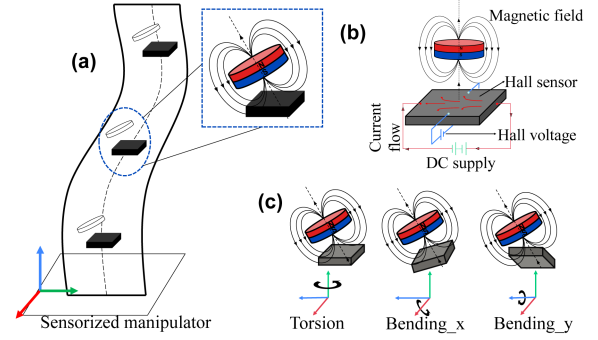

Fig. 1. Overview of the sensing method. (a) The arrangement of the magnet-sensor assembly. (b) The Hall Effect principle of operation. (c) The pose of the magnet relative to the sensor during deformations.
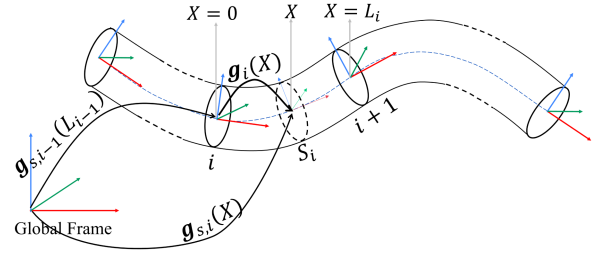

Fig. 2. Kinematics model of PCAS rod showing recursive kinematic computation in the ith division.

- We propose a simple design (Fig. 1) that embeds a single sensor and a magnet in every segment of the soft manipulator, enabling the localized estimation of local angular strains, including torsion.
- Through exploring different configurations of magnet-sensor pairs, we identified optimized design parameters that enhance scalability and ease of fabrication. Our findings include a unique configuration where the magnet is offset from the backbone and tilted, enabling a direct one-to-one mapping between angular strains and the magnetic field.
- We employed a neural network that processes magnetic field data from the sensor to predict all three angular strains. These predicted strains serve as input to our shape reconstruction based on the Piece-wise Constant Angular Strain (PCAS) model. PCAS can be considered a special case of Piecewise Constant Strain [25] or the polynomial angular strain parameterization [13], where each segment is restricted to a constant angular strain.
- We developed single and three-segment tendon-driven soft manipulators to experimentally validate our approach, demonstrating successful shape reconstruction for complex deformations.

The remainder of this letter is organized as follows. Section II presents the methodology, covering the kinematic models of PCAS, sensor design parameter optimization, and prototype fabrication. Section III describes the neural network model to estimate the strains and validates its effectiveness. Section IV discusses the shape estimation (proprioception) of the manipulator by combining the neural network and kinematic models. Finally, conclusions are provided in Section V.

II. SENSOR OPTIMIZATION AND INTEGRATION

When the soft manipulator, embedded with a magnet and sensor, deforms through twisting or bending, the resulting strain relatively transforms the magnet from its initial position and orientation. Shape reconstruction involves mapping the measured magnetic fields to the corresponding angular strains, followed by applying a kinematic model to compute the manipulator's shape from these strains.

A. Strain-Based Shape Reconstruction

Our shape reconstruction method builds on the Geometric Variable Strain (GVS) model [26], [27], a strain-based Cosserat rod framework that accounts for twisting, bending, stretching, and shearing. The manipulator is modeled as a continuum of rigid cross-sections along a curvilinear axis $X \in [0, L]$, with the strain field $\xi(X) \in \mathbb{R}^6$ parameterized using basis functions.

$$\boldsymbol{\xi}(X, \boldsymbol{q}) = \boldsymbol{\Phi}_\xi(X)\boldsymbol{q} + \boldsymbol{\xi}^*, \tag{1}$$

where $\boldsymbol{q} \in \mathbb{R}^n$ is the vector of generalized coordinates of dimension n and $\boldsymbol{\Phi}_\xi(X) \in \mathbb{R}^{6 \times n}$ is the basis function which spans the strain field, and $\boldsymbol{\xi}^*$ represents the strain in the reference state of the manipulator. If the rod is straight in the reference configuration, we have $\boldsymbol{\xi}^* = [0\ 0\ 0\ 1\ 0\ 0]^T$. Furthermore, if the strain field is constant and only has angular components we have $\boldsymbol{\Phi}_\xi = [\boldsymbol{I}_3\ \boldsymbol{0}^{3 \times 3}]^T$ and $n = 3$. This allows the manipulator to be represented as a series of segments, each modeled as a constant angular strain rod. We refer to this model as the Piecewise Constant Angular Strain (PCAS), which focuses on capturing the bending and torsional strains while assuming that the influence of shear and elongation is negligible.

Consider the schematic of a manipulator consisting of N PCAS segments as illustrated in Fig. 2. The kinematic map from frame i to the frame of any point $X \in [0,\ L_i]$ on the ith segment is expressed as the exponential map of the screw strain vector $\boldsymbol{\xi}$, represented mathematically as:

$$\boldsymbol{g}_i(X) = \exp\left(\widehat{X\boldsymbol{\xi}}\right). \tag{2}$$

where L_i is the length of the segment, the operator $\widehat{(\bullet)}$ indicates the isomorphism from $\mathbb{R}^6$ to $\mathfrak{se}(3)$, and the homogeneous transformation matrix $\boldsymbol{g}$ is given by:

$$\boldsymbol{g}_i = \begin{bmatrix} \boldsymbol{R}_i & \boldsymbol{r}_i \\ \boldsymbol{0} & 1 \end{bmatrix}, \tag{3}$$

The analytical formula of the exponential map of $\mathfrak{se}(3)$ is provided in the Appendix. The transformation from the global frame can be recursively computed according to:

$$\boldsymbol{g}_{s,i}(X) = \boldsymbol{g}_{s,i-1}(L_{i-1})\boldsymbol{g}_i(X) \tag{4}$$

B. Sensor Design Optimization

Here, we outline the procedure employed to determine the optimal design parameters that enable our sensorized manipulator to estimate angular strains from measured magnetic fields. A simpler approach to modeling magnetic field is the magnetic
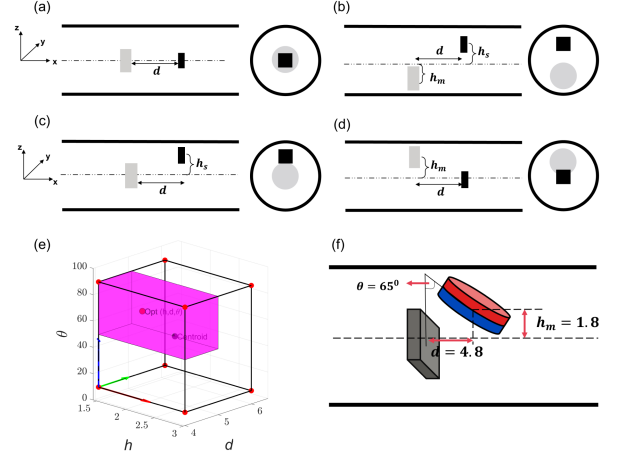

Fig. 3. Investigation on the design configuration: (a)–(d) The various possible configurations for the sensor-magnet pair, (e) hypercube for the grid search optimization, (f) schematic of the optimized design configuration.

TABLE I
RANGE OF VALUES FOR THE INVESTIGATION

Parameter	Symbol	Range	Unit
Torsion	ξ_1	[-30,30]	Rad/m
Bending about y-axis	ξ_2	[-30,30]	Rad/m
Bending about z-axis	ξ_3	[-30,30]	Rad/m
Magnet offset	h_m	[1.5,3]	mm
Magnet tilt angle	θ	[10,90]	Degrees
Magnet-sensor gap	d	[4,6]	mm

dipole model, which relies on assumptions such as a large sensor-magnet distance relative to the magnet's dimensions [28]. Since these assumptions do not hold in our setup, we utilize the Python package, *Magpylib* [29], which can simulate 3-axis magnetic fields for any pose. The simulated magnetic fields depend on the design parameters (the relative position and orientation when the robot is undeformed) and the strain between the sensor and the magnet. The design parameters include the magnet-sensor gap d, the offsets from the centerline, h (this can either be the magnet offset, h_m, or the sensor offset, h_s) Four possible arrangements of the magnet and sensor are shown in Fig. 3.

As shown in prior work [30], [31], aligning the magnet axis with the manipulator's backbone prevents torsion sensing due to field symmetry, leading to the exclusion of configurations in Fig. 3(a) and (c). Configurations 3(b) and 3(d), with the magnet offset from the backbone, enable torsion sensing. To reduce the manipulator diameter and ease fabrication, configuration 3(d) was selected. While it allows torsion estimation, it does not guarantee a one-to-one mapping between angular strains and magnetic fields. Thus, the magnet's tilt angle θ was introduced as an additional design parameter. A sensitivity analysis was conducted using known strain inputs (Table I), with combinations of d, h, and θ evaluated via PCAS and Magpylib to identify the optimal configuration.

The parameter ranges used in each configuration are listed in Table I. These were selected to keep the magnetic field within the sensor's operating range, avoiding saturation and physical contact between the sensor and magnet during deformation. To assess the mapping quality between simulated magnetic fields

TABLE II
GRID SEARCH OPTIMIZATION

h (mm)	d (mm)	θ (^{0})	Ω (10^{-3})
1.5	4	10	2.6
1.5	4	90	0.44
1.5	6	10	0.33
1.5	6	90	11.3
3	4	10	0.311
3	4	90	20.6
3	6	10	0.15
3	6	90	9.6
$h_{centroid}$	$d_{centroid}$	$\theta_{centroid}$	0.92
$h_{opt} = 1.8$	$d_{opt} = 4.8$	$\theta_{opt} = 65$	**23.6**

and applied angular strains, a sensitivity-based cost function Ω was defined,

$$\Omega = \min\left(\frac{\|\boldsymbol{B}_i - \boldsymbol{B}_j\|}{\|\boldsymbol{\xi}_i - \boldsymbol{\xi}_j\|}\right), \quad (5)$$

where $\boldsymbol{\xi} \in \mathbb{R}^3$ is the applied angular strain, $\boldsymbol{B} \in \mathbb{R}^3$ is the magnetic field. The indices i and j represent two distinct measurement instances, where i iterates over all readings, and j spans the remaining readings for pairwise comparisons. The expression is evaluated for all unique pairs, ensuring $i \neq j$ with $i, j \in \{1, \ldots, n\}$, where n is the total number of simulations. The computed Ω represents the worst-case sensitivity of a configuration. A high Ω value indicates strong sensitivity—where small strain changes produce large magnetic field variations—favoring a one-to-one mapping. Conversely, a low Ω implies poor sensitivity and difficulty in distinguishing strain states.

The optimal configuration was selected by maximizing Ω over parameters d, h, and θ. Table II reports results for configurations located at the vertices and centroid of the parameter cube (Fig. 3(e)), for brevity. The highest-performing configurations lie within the magenta-highlighted quarter of the cube. The design parameters selected for our prototype, listed in the last row of Table II, fall within this optimal region. As shown in Fig. 3(f), tilting the magnet is essential, as low inclination angles lead to reduced sensitivity, with Ω approaching zero as the angle nears zero—highlighting the importance of magnet tilt for achieving a one-to-one mapping.

C. Fabrication and Integration

We created a single and three-segment sensor-embedded manipulators using the optimized design parameters. The fabrication process is illustrated in Fig. 4. Frames a-e of the figure depict the fabrication of the single-segment manipulator. 3D-printed disks, designed to fit within the mold, were utilized to securely hold the magnet and sensor, as shown in Fig. 4(b). The disks were made smaller than the manipulator diameter to allow seamless embedding of the sensor-magnet pair in silicone. Silicone was gravity-filled into the mold and cured, after which the embedded manipulator—measuring 50 mm in length and 15 mm in diameter—was extracted. Fig. 4(f) shows three single-segment manipulators that are connected in series to create a longer manipulator equipped with three sensor-magnet pairs. Each segment was molded to a final length of 80 mm, giving the three-segment manipulator a total length of 240 mm. Black rings were embedded to mark sensor locations. Both prototypes
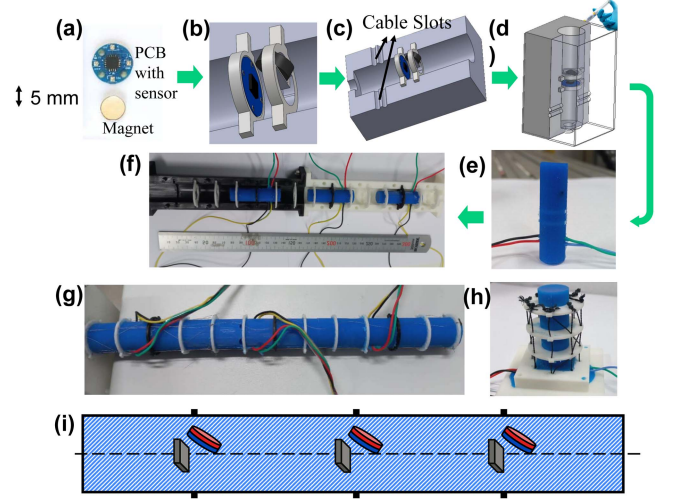

Fig. 4. Fabrication process: (a) Fabricated PCB with 3-axis sensor and magnet. (b)–(e) fabrication of the single-segment manipulator. (f) Building of the three single-segment manipulator, (g) Actuated three-segment manipulator. (h) Actuated single-segment manipulator. (i) cross-sectional layout of the sensorized manipulator.

use cable-driven actuation, with 3D-printed rings along the manipulator to guide actuator cables, ensuring uniform force distribution and consistent bending moments. The final diameter of both manipulators is 20 mm. The manipulators were fabricated using SmoothOn Mold Star 30 silicone rubber, which exhibits elastic behavior within the applied strain range. A cylindrical neodymium magnet (N52 grade, 6 mm diameter, 2 mm height, axially magnetized) was selected for its shape compatibility and minimal effect on the manipulator's mechanical properties.

A custom 10 mm × 1 mm circular PCB was developed to mount the MLX90393 3-axis sensor (Fig. 4(a)). The sensor measures3 3 mm, with a 5–50 mT dynamic range and 16-bit resolution. Wire slots were added beside the mold (Fig. 4(c)) for connectivity. I²C protocol was used to interface the sensor with the microcontroller, allowing communication with all sensor-magnet pairs using only four wires.

III. STRAIN ESTIMATION AND VALIDATION

The proprioception method was validated on single- and three-segment manipulators under various deformation modes (C-shape, S-shape, torsion, and combined modes). Magnetic field data were collected at 90 Hz using an Arduino, while ground truth deformation was captured via a 24-camera OptiTrack system (OptiTrack Prime 22x) at 100 Hz. Reflective markers were mounted for accurate tracking, and 3D angular strains were estimated using marker data and the PCAS model to train the neural network. The experimental setup is depicted in Fig. 5.

A. Strain Prediction Network

While *Magpylib* can provide a forward map from displacement to magnetic field, developing an inverse map to calculate angular strains from magnetic field measurements is complex and non-linear. Instead, data-driven methods like machine learning offer a promising alternative. These methods can learn the relationships between those physical quantities and can also
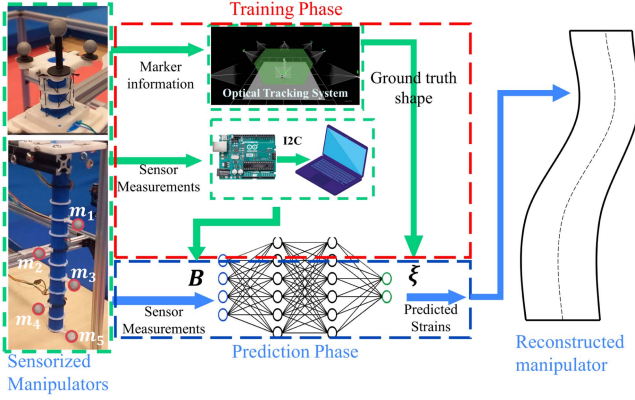
Fig. 5. Experimental Setup: The left frame comprises the sensorized manipulators, the middle-top involves the training phase (red outline), the middle-bottom represents the prediction phase (blue outline), and the far right depicts the reconstructed shape of the manipulator.
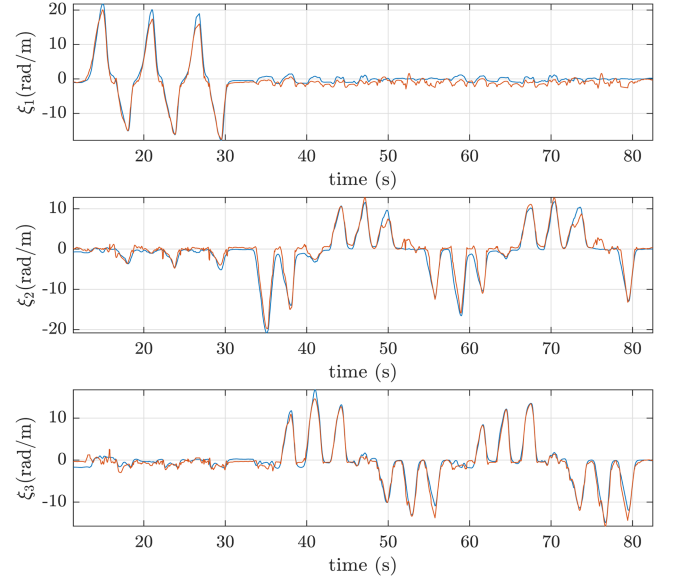

Fig. 6. Plots of actual and predicted angular strains for the single-segment manipulator. The ground truth of the strains is plotted in blue, while the predicted strain is plotted in red.

adjust for minor fabrication errors. Machine learning has already been used in soft robotic systems to estimate 2-axis bending and stretching [11], [15]. In our work, we use a machine-learning approach to predict 3D angular strains based on the magnetic field measured by a sensor, effectively serving as a mapping between sensor measurements and the manipulator's deformation state. We use a fully connected multilayer perceptron to define a function, f_W, that maps the magnetic field readings to angular strain values. The input to the network is a 3D magnetic field vector from a Hall effect sensor, $B_i = [B_x, B_y, B_z] \in \mathbb{R}^3$, and the output is a vector of the estimated angular strains, $\xi_i = [\xi_1, \xi_2, \xi_3] \in \mathbb{R}^3$. The goal is to find the best set of weights needed by the function $f_W(B_i)$ to predict the strains. After training, the model can predict strain values from new magnetic field data. We used 70% of the data for training and the remaining 30% for validation and testing. The network has three hidden layers with 10, 8, and 6 neurons, respectively, each using the hyperbolic tangent sigmoid (tansig) activation function. We measured how well the model performs using the mean square error (MSE). All network design, training, and testing were done using MATLAB's Deep Learning Toolbox.

Stray magnetic fields, including the Earth's magnetic field, can affect calibration if the variation caused by sensor orientation changes is comparable to that induced by deformation. We observed that the variation in the magnetic field due to orientation alone is approximately 37 μT, whereas the average field variation resulting from deformation during our experiments is substantially higher—in the order of 1500 μT. This indicates that orientation-induced variation might account for less than 3% of the total field variation. Therefore, the calibration of our strain prediction network is robust to changes in the manipulator's orientation.

B. Single-Segment Manipulator

Following the PCAS method described in Section II-A and the training network described in Section III-A, we evaluate the results of the single-segment manipulator. The manipulator was secured in an upright position as shown in Fig. 5. A rigid

body frame was created using the attached markers, enabling the computation of the transformation matrix from the robot's tip to the base. Given the transformation g_{tr} from the base to the tip of the manipulator, obtained from the tracking system, the screw strain can be computed using the logarithmic map as follows:

$$\boldsymbol{\xi}_1 = \frac{1}{L_1} \log(\boldsymbol{g}_{tr})^\vee. \tag{6}$$

where L_1 is the length of the manipulator and the formula of the logarithmic map is provided in the Appendix. The angular strains can be extracted from $\boldsymbol{\xi}_1$.

The manipulator uses two helically routed cables (pitch: 10 cm) for torsional actuation and eight straight, symmetrically placed cables for 2-axis bending, routed parallel to the centerline from base to tip. Fig. 5 shows the initial reference configuration of the manipulator with 10 actuators. It was randomly actuated with combined torsion and 2-axis bending. After 5 minutes, tracking and sensor data were aligned and processed, yielding 28,450 samples for training the neural network, as described in Section III-A.

To evaluate the predictor model, a new experiment was performed involving clockwise and counterclockwise twisting, followed by bending in a circumferential pattern around the manipulator. Fig. 6 shows the comparison between predicted and true strains. The maximum torsional error was 3 rd/m (mean: 0.89 rd/m), while bending errors were 3.4 rd/m (y-axis) and 3 rd/m (z-axis), with mean absolute errors of 0.82 and 0.6 rd/m, respectively. Given the strain range of 30 rd/m, the prediction errors are within acceptable limits.

The material does not exhibit significant viscoelastic effects over the timescales considered in our experiments. To confirm this, we actuated the manipulator to a maximum strain of approximately 20 rad/m at different strain rates and observed minimal
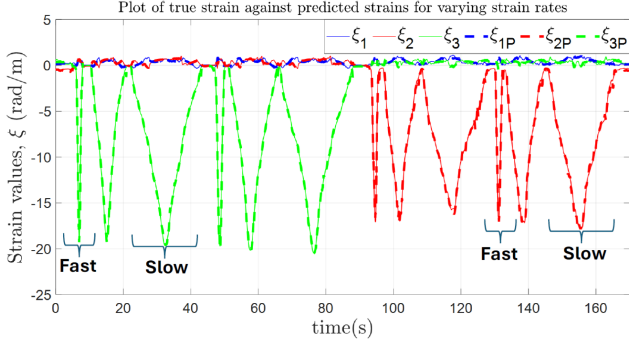
Fig. 7. Effect of strain rate on the manipulator. Solid lines represent strains measured using the tracking system, while dashed lines indicate strains predicted by the sensor-based model (denoted with subscript p).
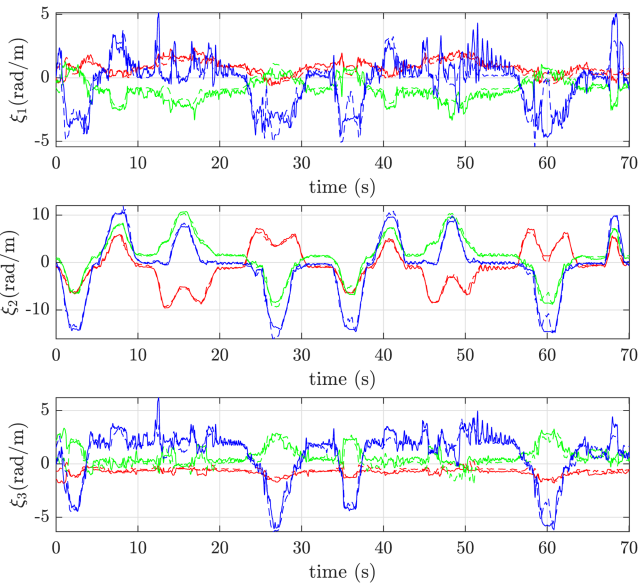

Fig. 8. Plots showing the actual and predicted angular strains for the three-segment manipulator. The ground truth strains are plotted in solid, while the predicted strains are in dashed lines. Red, green, and blue plots indicate the strains in the first, second, and third segments respectively.

deviation in sensor predictions. As shown in Fig. 7, the sensing method remains robust to strain-rate variations.

C. Three-Segment Manipulator

For the three-segment manipulator, acquiring the angular strains needed for model training and validation is quite challenging. To address this, we adopted the estimation method from [32], which aligns model-predicted marker positions with tracking data. Five reflective markers, spaced 20 mm apart from the tip, were used (Fig. 5). Assuming a model composed of three PCAS segments, the measured marker positions p^m, from the tracking system were used to estimate strains q^e via a minimization problem,

$$\min_{q^e} \ \Xi(q^e) = \Sigma_{i=1}^5 \| p_i^m - p_i(q^e) \|^2 \tag{7}$$
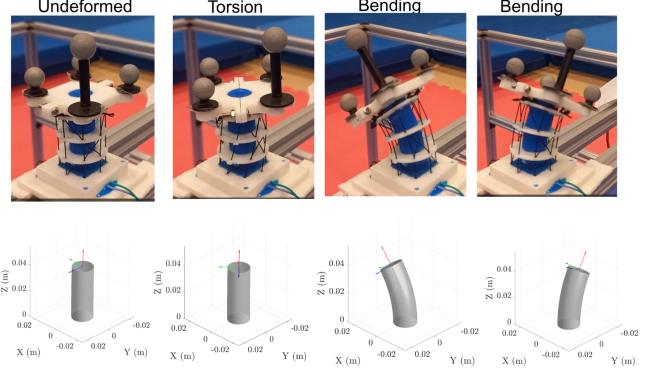

Fig. 9. Snapshots of the deformed single-segment manipulator alongside the corresponding still images of the reconstructed manipulator shapes.

where we denote the estimated position of the markers as $[p_i^T(q^e)\ 1]^T = g_s(q^e)[p_{i,l}^T\ 1]^T$, with $p_{i,l}$ representing the position vector of the marker in the local frame, and $g_s(q^e)$ is computed using (4).

The three-segment manipulator used the same torsional cable routing as the single-segment design, confined to the proximal segment to control tip pose during twisting. For bending, the manipulator is equipped with two distinct sets of straight cables, each consisting of 4 cables arranged parallel to the manipulator's centerline. The first set is anchored at the tip of the proximal segment, while the second set extends to the tip of the manipulator. C-shaped bending was achieved by actuating one of the cables routed from the second set. For the S-shaped configuration, two opposing cables from both sets were actuated simultaneously. The experiment spanned approximately 25 minutes, during which various deformations were sequentially obtained. The sampling rate remained consistent with that used in the single-segment manipulator experiment, resulting in the collection of 150,054 data points. The training-to-testing ratio was maintained at the same proportion as that employed in the single-segment manipulator experiment.

Fig. 8 presents results from a new experiment involving C- and S-shaped bending about the y-axis, comparing neural network predictions with tracking-based strain estimates across all three manipulator segments. The model shows strong quantitative agreement. Maximum absolute errors were 5.17 rd/m (torsion), 4.61 rd/m (bending y), and 3.39 rd/m (bending z), with respective mean errors of 0.73, 0.48, and 0.53 rd/m. Occasional error spikes are attributed to tracking inaccuracies, while average errors remain below 5% of the total strain range.

IV. PROPRIOCEPTION

In this section, we demonstrate the effectiveness of our methodology in estimating the manipulator's shape, leveraging the neural network and kinematic models discussed in the previous sections.

A. Single-Segment Manipulator

To demonstrate shape reconstruction from the sensorized manipulator, we conducted new experiments and using the
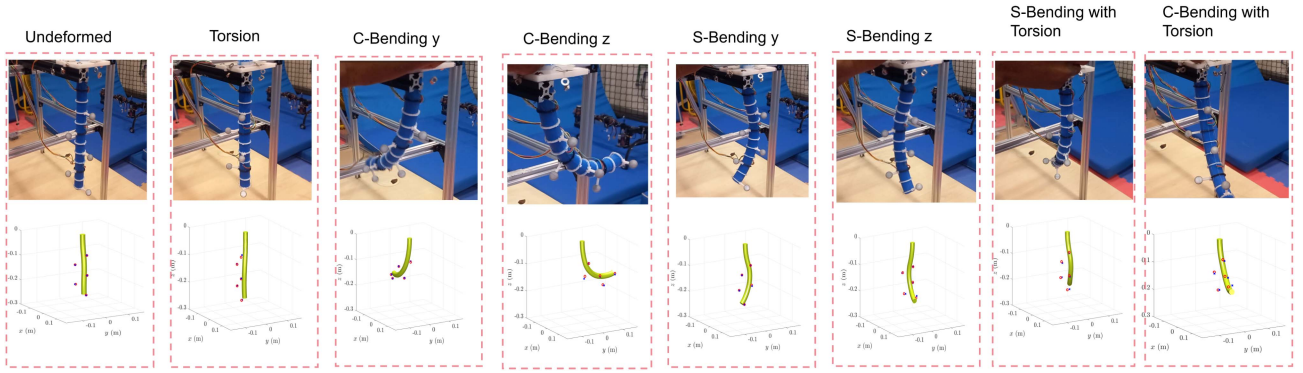
Fig. 10.　Snapshots of the deformed three-segment manipulator alongside the corresponding still images of the reconstructed manipulator shapes.

TABLE III
ESTIMATION ERROR THREE SEGMENT MANIPULATOR

Deformation modes	MSE Marker Positions (mm)				
	$m1$	$m2$	$m3$	$m4$	$m5$
C & S bending (y-axis)	4.3	4.3	3.5	4.3	5.5
C & S bending (y & z axes)	6.1	5.9	6.5	7.0	9.5
C bending (y & z axes); Torsion	5.7	5.3	5.1	6.0	7.8
S bending (y & z axes); Torsion	4.1	5.1	6.3	7.5	9.0
Combined bending with Torsion	3.4	5.5	6.5	8.9	11.5

neural network, the strains were predicted. We applied (2) to compute the manipulator's shape. The estimated shape was then compared qualitatively with the recorded shape and quantitatively with the tracked tip pose. Fig. 9 shows some snapshots together with the reconstructed shape, illustrating torsion and bending along two axes. The mean tip position error recorded was less than 1 mm while the maximum tip error was 3.1 mm. Readers can view the video comparison in the supplementary material.

B. Three-Segment Manipulator

To evaluate the performance of the predictor model for the three-segment manipulator, we conducted new controlled experiments involving pure bending, pure torsion as well as combined bending and torsion. For pure bending, the two modes of deformations described in Section III-C were achieved. The combined bending and torsion involved first bending the manipulator into a C- or S-shape, followed by the application of torsion while maintaining the manipulator in the bent state. Using the neural network-predicted strains and (4) and (2), we reconstructed the manipulator's shape. The recorded video of the deformation offers a qualitative comparison, while the tracked marker positions are compared with the model-predicted positions for quantitative analysis.

Fig. 10 shows the snapshots from the shape reconstruction of the three-segment manipulator undergoing complex deformations. Additionally, Table III presents the mean squared error (MSE) for the manipulator's marker positions under these deformation modes.

The maximum marker position error of 11 mm, recorded from the marker closest to the tip, represents less than 5% of the manipulator's total length. For a video comparison, readers may refer to the supplementary material.

V. DISCUSSION AND CONCLUSIONS

We present a novel method for embedding Hall effect sensors and magnets in soft manipulators to estimate 3-axis angular strains. The sensor is aligned with the manipulator's backbone, while the magnet is tilted and offset. Magpylib simulations and the PCAS model were used to optimize the design for low-cost, scalable sensorization. Validation on single- and three-segment prototypes showed high prediction accuracy, with marker position errors under 2% and 5%, respectively. This is the first demonstration of estimating angular strains—including torsion—using a single embedded Hall effect sensor and magnet, with potential for underwater applications due to the protected integration.

The proposed Hall-effect sensing approach has its own inherent limitations. Hall-effect sensors are susceptible to variations in magnetic fields, particularly when operating in close proximity to ferromagnetic materials. The PCAS sensing approach also has a fundamental limitation: it can only capture angular deformations, which is sufficient for slender soft bodies that can be modeled as inextensible Kirchhoff rods. However, in soft bodies that undergo elongation and shear under high deformation or dynamic loading conditions, this may result in inaccurate estimations. While the presence of nearby ferromagnetic materials is an inherent limitation of Hall-effect sensing, the use of multiple sensors can help mitigate challenges in capturing elongation and shear, enhance overall sensing accuracy, and enable the estimation of higher-order deformation modes. We intend to explore this direction in future work. While the proposed approach is applicable to Hall effect sensing in slender rods, the trained neural network model is specific to the manipulator's design, material properties, and deformation range. Therefore, each embedded sensor system must be individually characterized prior to deployment. Future work will explore the performance of our sensor system under dynamic conditions and its potential integration into closed-loop control systems, positioning our technique as a promising paradigm for proprioception in soft robotics.

APPENDIX A

Exponential map of Lie algebra $\mathfrak{se}(3)$:

$$\exp\left(\widehat{X\boldsymbol{\xi}}\right) = I_4 + \widehat{X\boldsymbol{\xi}} + \frac{1-\cos(\theta)}{\theta^2}\left(\widehat{X\boldsymbol{\xi}}\right)^2 + \frac{\theta - \sin(\theta)}{\theta^3}\left(\widehat{X\boldsymbol{\xi}}\right)^3$$

where $\theta = \|[\boldsymbol{I}_3\ \boldsymbol{0}^{3\times3}]\boldsymbol{\xi}\|$.

Logarithmic map of Lie algebra $\mathfrak{se}(3)$:

$$\log(\boldsymbol{g}) = \frac{1}{8}\csc^3\left(\frac{\theta}{2}\right)\sec\left(\frac{\theta}{2}\right)\Bigg((\theta\cos(2\theta) - \sin(\theta))\,\boldsymbol{I}_4$$
$$- (\theta\cos(\theta) + 2\theta\cos(2\theta) - \sin(\theta) - \sin(2\theta))\,\boldsymbol{g}$$
$$+ (2\theta\cos(\theta) + \theta\cos(2\theta) - \sin(\theta) - \sin(2\theta))\,\boldsymbol{g}^2$$
$$- (\theta\cos(\theta) - \sin(\theta))\,\boldsymbol{g}^3\Bigg)$$

where θ satisfies $\mathrm{Tr}(\boldsymbol{g}) = 2(1 + \cos(\theta))$ for $-\pi < \theta < \pi$.

REFERENCES

[1] H. Wang, M. Totaro, and L. Beccai, "Toward perceptive soft robots: Progress and challenges," *Adv. Sci.*, vol. 5, no. 9, 2018, Art. no. 1800541.

[2] F. Stella, C. D. Santina, and J. Hughes, "Soft robot shape estimation with IMUs leveraging PCC kinematics for drift filtering," *IEEE Robot. Autom. Lett.*, vol. 9, no. 2, pp. 1945–1952, Feb. 2024.

[3] G. Thomas, B. Thuruthel, C. S. Laschi, and M. T. Tolley, "Soft robot perception using embedded soft sensors and recurrent neural networks," *Sci. Robot.*, vol. 4, no. 26, 2019, Art. no. eaav1488.

[4] S. Tian, B. G. Cangan, S. E. Navarro, A. Beger, C. Duriez, and R. K. Katzschmann, "Multi-tap resistive sensing and FEM modeling enables shape and force estimation in soft robots," *IEEE Robot. Autom. Lett.*, vol. 9, no. 3, pp. 2830–2837, Mar. 2024.

[5] G. Gerboni, A. Diodato, G. Ciuti, M. Cianchetti, and A. Menciassi, "Feedback control of soft robot actuators via commercial flex bend sensors," *IEEE/ASME Trans. Mechatron.*, vol. 22, no. 4, pp. 1881–1888, Aug. 2017.

[6] J. Hughes, F. Stella, C. D. Santina, and D. Rus, "Sensing soft robot shape using IMUs: An experimental investigation," in *Proc. Exp. Robot.: 17th Int. Symp.*, 2021, pp. 543–552.

[7] D. Feliu-Talegon, Y. A. Adamu, A. T. Mathew, A. Y. Alkayas, and F. Renda, "Advancing soft robot proprioception through 6D strain sensors embedding," *Soft Robot.*, 2025, doi: 10.1089/soro.2024.0017.

[8] Y. Toshimitsu, K. W. Wong, T. Buchner, and R. Katzschmann, "SoPrA: Fabrication & dynamical modeling of a scalable soft continuum robotic arm with integrated proprioceptive sensing," in *Proc. IEEE/RSJ Int. Conf. Intell. Robots Syst.*, 2021, pp. 653–660.

[9] J. Yi, X. Zhu, L. Shen, B. Sun, and L. Jiang, "An orthogonal curvature fiber Bragg grating sensor array for shape reconstruction," in *Proc. Int. Conf. Intell. Comput. Sustain. Energy Environ.*, 2010, pp. 25–31.

[10] R. K. Kramer, C. Majidi, R. Sahai, and R. J. Wood, "Soft curvature sensors for joint angle proprioception," in *Proc. IEEE/RSJ Int. Conf. Intell. Robots Syst.*, 2011, pp. 1919–1926.

[11] M. D. Mitchell, F. E. Hurley, and C. D. Onal, "Fast probabilistic 3-D curvature proprioception with a magnetic soft sensor," in *Proc. IEEE 17th Int. Conf. Automat. Sci. Eng.*, 2021, pp. 215–220.

[12] Z. Xie, F. Yuan, Z. Liu, Z. Sun, E. M. Knubben, and L. Wen, "A proprioceptive soft tentacle gripper based on crosswise stretchable sensors," *IEEE/ASME Trans. Mechatron.*, vol. 25, no. 4, pp. 1841–1850, Aug. 2020.

[13] A. L. Orekhov, E. Z. Ahronovich, and N. Simaan, "Lie group formulation and sensitivity analysis for shape sensing of variable curvature continuum robots with general string encoder routing," *IEEE Trans. Robot.*, vol. 39, no. 3, pp. 2308–2324, Jun. 2023.

[14] D. Feliu-Talegon, A. T. Mathew, A. Y. Alkayas, Y. A. Adamu, and F. Renda, "Dynamic shape estimation of tendon-driven soft manipulators via actuation readings," *IEEE Robot. Autom. Lett.*, vol. 10, no. 1, pp. 780–787, Jan. 2025.

[15] T. Baaij et al., "Learning 3D shape proprioception for continuum soft robots with multiple magnetic sensors," *Soft Matter*, vol. 19, no. 1, pp. 44–56, 2023.

[16] S. Ozel, N. A. Keskin, D. Khea, and C. D. Onal, "A precise embedded curvature sensor module for soft-bodied robots," *Sensors Actuators A: Phys.*, vol. 236, pp. 349–356, 2015.

[17] H. Guo et al., "Continuum robot shape estimation using permanent magnets and magnetic sensors," *Sensors Actuators A: Phys.*, vol. 285, pp. 519–530, 2019.

[18] S. Song, Z. Li, H. Yu, and H. Ren, "Electromagnetic positioning for tip tracking and shape sensing of flexible robots," *IEEE Sensors J.*, vol. 15, no. 8, pp. 4565–4575, Aug. 2015.

[19] C. F. Costa and J. C. Reis, "End-point position estimation of a soft continuum manipulator using embedded linear magnetic encoders," *Sensors*, vol. 23, no. 3, 2023, Art. no. 1647.

[20] R. Takano, H. Mochiyama, and N. Takesue, "Real-time shape estimation of Kirchhoff elastic rod based on force/torque sensor," in *Proc. IEEE Int. Conf. Robot. Automat.*, 2017, pp. 2508–2515.

[21] C. Alessi, C. Agabiti, D. Caradonna, C. Laschi, F. Renda, and E. Falotico, "Rod models in continuum and soft robot control: A review," 2024, *arXiv:2407.05886*.

[22] N. Nakagawa and H. Mochiyama, "Real-time shape estimation of an elastic rod using a robot manipulator equipped with a sense of force," in *Proc. 2018 IEEE/RSJ Int. Conf. Intell. Robots Syst.*, 2018, pp. 8067–8073.

[23] K. B. Reed, A. M. Okamura, and N. J. Cowan, "Modeling and control of needles with torsional friction," *IEEE Trans. Biomed. Eng.*, vol. 56, no. 12, pp. 2905–2916, Dec. 2009.

[24] R. Xu, A. Yurkewich, and R. V. Patel, "Curvature, torsion, and force sensing in continuum robots using helically wrapped FBG sensors," *IEEE Robot. Autom. Lett.*, vol. 1, no. 2, pp. 1052–1059, Jul. 2016.

[25] F. Renda, F. Boyer, J. Dias, and L. Seneviratne, "Discrete Cosserat approach for multisection soft manipulator dynamics," *IEEE Trans. Robot.*, vol. 34, no. 6, pp. 1518–1533, Dec. 2018.

[26] A. T. Mathew, D. Feliu-Talegon, A. Y. Alkayas, F. Boyer, and F. Renda, "Reduced order modeling of hybrid soft-rigid robots using global, local, and state-dependent strain parameterization," *Original Art. Int. J. Robot. Res.*, vol. 44, no. 1, pp. 129–154, 2024.

[27] F. Boyer, V. Lebastard, F. Candelier, and F. Renda, "Dynamics of continuum and soft robots: A strain parameterization based approach," *IEEE Trans. Robot.*, vol. 37, no. 3, pp. 847–863, Jun. 2021.

[28] F. Y. Wu, S. Foong, and Z. Sun, "A hybrid field model for enhanced magnetic localization and position control," *IEEE/ASME Trans. Mechatron.*, vol. 20, no. 3, pp. 1278–1287, Jun. 2015.

[29] M. Ortner, L. Gabriel, and C. Bandeira, "Magpylib: A free Python package for magnetic field computation," *SoftwareX*, vol. 11, 2020, Art. no. 100466.

[30] Q. Nie and F. C. Sup, "A soft four degree-of-freedom load cell based on the Hall effect," *IEEE Sensors J.*, vol. 17, no. 22, pp. 7355–7363, Nov. 2017.

[31] D. S. Chathuranga, Z. Wang, Y. Noh, T. Nanayakkara, and S. Hirai, "A soft three axis force sensor useful for robot grippers," in *Proc. 2016 IEEE/RSJ Int. Conf. Intell. Robots Syst.*, 2016, pp. 5556–5563.

[32] A. Y. Alkayas, A. T. Mathew, D. Feliu-Talegon, P. Deng, T. G. Thuruthel, and F. Renda, "Soft synergies: Model order reduction of hybrid soft-rigid robots via optimal strain parameterization," *IEEE Trans. Robot.*, vol. 41, pp. 1118–1137, 2025.